International Journal of Biological Macromolecules 82 (2016) 702–710

Contents lists available at ScienceDirect

International Journal of Biological Macromolecules

journal homepage: www.elsevier.com/locate/ijbiomac

Magnetic chitosan–graphene oxide composite for anti-microbial and dye removal applications

Yan Jiang[a], Ji-Lai Gong[a,*], Guang-Ming Zeng[a,*], Xiao-Ming Ou[b], Ying-Na Chang[a], Can-Hui Deng[a], Jing Zhang[a], Hong-Yu Liu[a], Shuang-Yan Huang[c]

[a] College of Environmental Science and Engineering, Key Laboratory of Environmental Biology and Pollution Control, Ministry of Education, Hunan University, Changsha 410082, PR China
[b] China National Engineering Research Center for Agrochemicals, Hunan Research Institute of Chemical Industry, Changsha 410014, PR China
[c] State Key Laboratory for Chemo/Biosensing and Chemometrics, College of Chemistry and Chemical Engineering, Hunan University, Changsha 410082, PR China

ARTICLE INFO

Article history:
Received 1 August 2015
Received in revised form 22 October 2015
Accepted 8 November 2015
Available online 12 November 2015

Keywords:
Antibacterial
Adsorption
Chitosan

ABSTRACT

Magnetic chitosan–graphene oxide (MCGO) nanocomposite was prepared as a multi-functional nanomaterial for the applications of antibacterial and dye removal. The nanocomposite was characterized by scanning electronic microscope (SEM), transmission electron microscopy (TEM), X-ray diffraction (XRD) and Fourier transform infrared spectrometer (FTIR). The antibacterial performance for MCGO against *Escherichia coli* was varied depending on the concentration of MCGO. SEM images of *E. coli* cells demonstrated that the antimicrobial performance of MCGO nanocomposite was possibly due to the damage of cell membrane. This work also explored MCGO's adsorption performance for methyl orange (MO). The experimental parameters including adsorbent mass, pH value, contact time and concentration of MO on the adsorption capacity were investigated. The maximum adsorption capacity of MCGO for MO was 398.08 mg/g. This study showed that the MCGO offered enormous potential applications for water treatment.

1. Introduction

Water pollution has become a serious problem, many kinds of pollutions existed in water environment, including microorganism, metal ions, organics, and so on. With the increasingly serious water pollution, the exploitation of novel and multifunctional materials has received adequate attention over the past decade [1–5]. Chitin is the second most abundant polymer in nature after cellulose, and can be extracted from arthropods, crustaceans, fungi, and yeast [6]. Chitosan (CS), a carbohydrate biopolymer that has hydroxyl groups and highly reactive amino groups, synthesized from the deacetylation of chitin. With its excellent antimicrobial, non-toxicity, biocompatibility, biodegradability and adsorption properties [7–9], CS and its derivatives have been widely used in water treatment, sensors, medicine, drug delivery, metal chelating agents, food packaging, and so on [10–14]. Recently, a large number of scientists investigated the CS adsorption property toward reactive dye [9,15] and heavy metal [16,17]. Additionally, the toxic effects of CS toward bacterium also received enormous attention [18–20]. However, chitosan solubility in acid solution limited its applications. Therefore, it is necessary to prepare functionalized chitosan derivatives to make it stable in acid solution [21].

Graphene oxide (GO) is a one-atom-thick sheet and two dimensional crystal of sp^2-bonded carbon atoms, and has attracted considerable attention since the experimental discovery of Novoselov et al. [22]. With its unique physical and chemical properties, such as the large specific area and extraordinary mechanical strength, GO has revealed a remarkable performance in the adsorption of dyes and support for catalyst [23,24]. Recent research has indicated that GO also exerted antibacterial properties. Akhavan and Ghaderi [25] investigated the antibacterial properties of graphene oxide nano-walls and proposed that GO exerted antibacterial activity by damaging the cell membrane.

To date, there are several articles in literature on the adsorption and antibacterial properties by multi-functional materials. For example, Santhosh et al. [26] investigated the adsorption, photodegradation and antibacterial performance of graphene–Fe_3O_4 nanocompasite. They noted the nano-composite showed an excellent adsorption capacity (69 mg/g) toward lead ions and remained 97% degradation of methylene blue after 5 cycles. The antibacterial tests depicted a good antibacterial activity toward *Escherichia coli*

* Corresponding authors.
E-mail addresses: jilaigong@gmail.com (J.-L. Gong), zgming@hnu.edu.cn (G.-M. Zeng).

http://dx.doi.org/10.1016/j.ijbiomac.2015.11.021
0141-8130/

cells when treated with graphene–Fe_3O_4 nano-composite (only 22.33% of the cells were viable). Chella et al. [27] investigated the adsorption of lead and cadmium ions and cytotoxicity behavior toward *E. coli* cells using $MnFe_2O_4$–graphene composite and the results showed the extraordinary adsorption capacity (100 mg/g for lead and 76.90 mg/g for cadmium) and high antibacterial activity (82% cells loss). Mejias Carpio et al. [28] synthesized graphene oxide-ethylenediamine triacetic acid and also investigated their adsorption and antimicrobial properties. The results show that there are 92.3 ± 10% cell inactivation for *Bacillus subtilis* and 99.1 ± 1.3% cell inactivation for *Cupriavidus metallidurans*, and the adsorption capacity for Pb^{2+} and Cu^{2+} are 454.6 mg/g and 108.7 mg/g, respectively.

As previously reported, there are plenty of hydroxyl, epoxy and carboxyl groups on the basal plane and the edge of the sheets of GO [29], which makes it possible to form biocomposite by the formation of chemical bond between the carboxyl group of GO and the amine group of CS. Hence, some scientists have synthesized chitosan–graphene oxide composite to act as bio-adsorbents according to the favorable adsorption properties of CS and inherent properties of GO [21,29]. Additionally, the magnetic chitosan composite was synthesized by some scientists [30–32], and the properties of antibacterial and adsorption of magnetic chitosan were investigated. Furthermore, Fan et al. [33–35] synthesized magnetically separable magnetic chitosan/graphene oxide composite (MCGO) and investigated its adsorption properties for methyl blue and lead ions. However, to the best of our knowledge, there is no report to explore the antibacterial capacity and the adsorption action for methyl orange (MO) of MCGO nanocomposite. The synthesized MCGO nanocomposite will combine the adsorption and antibacterial performance of CS and GO and the separation convenience of iron oxide nanoparticle.

In the present study, the nanocomposite MCGO was synthesized and proposed to be used as a multi-functional material. The morphology and physicochemical properties of MCGO were characterized by scanning election microscopy (SEM), transmission electron microscopy (TEM), Fourier transform infrared spectrometer (FTIR) and X-ray diffraction (XRD) analysis. *E. coli* was chosen as a model bacterium due to its Gram-negative bacterium and widely being involved in water contamination [36]. We investigated the effect of material concentration on the antibacterial capacity of MCGO toward *E. coli*. At the same time, the adsorption performance was also investigated, where MO was employed as a representative pollutant, which is widely used in chemical, paints and leather industries [29,37]. The influence of various factors on adsorption, such as the adsorbent dosage, pH value, contact time and initial dye concentration was evaluated.

2. Materials and methods

2.1. Strains and chemicals

The bacterial strains used in this study was *E. coli* ATCC 25922 obtained from the China Center for Type Culture Collection (Beijing, China). The growth medium was maintained on LB agar slants at 4 °C. Graphite powder was purchased from Shanghai Jin-Shan-Ting new chemical factory (Shanghai, China). Chitosan with a degree of deacetylation above 90% was purchased from Sinopharm Chemical Reagent Co. (Shanghai, China). Methyl Orange was obtained from Tianjin Kermel Chemical Reagent Co. (Tianjin, China). All other reagents used in this study were analytical grade, and distilled water was used in the preparation of all solutions.

2.2. Preparation of graphene oxide (GO)

Graphene oxide (GO) was prepared according to the modified Hummer's method [38]. Briefly, 1 g graphite powder was added into a conical flask containing 23 mL H_2SO_4 and 0.5 g $NaNO_3$, followed by the addition of 3 g $KMnO_4$ with a slow speed under ice bath condition and agitation. Subsequently, the reaction was maintained at 35 °C for 1 h in water bath, then diluted with distilled water and controlled at 98 °C for 15 min. After reaction, the mixture was diluted to 140 mL with warm water (about 30 °C), with subsequent addition of 2.5 mL H_2O_2. Finally, the product (GO) was washed with distilled water for several times and then freeze dried for 48 h.

2.3. Synthesis of MCGO

Chitosan–graphene oxide (CGO) suspension was synthesized according to previous studies [39,40]. Briefly, chitosan aqueous solution was prepared by dissolving 0.5 g chitosan powder into 2.0% (v/v) acetic acid solution, and 0.1 g GO was dispersed in 20 mL distilled water with ultrasonication to form suspension. Then, the GO suspension was slowly added into the chitosan aqueous solution with vigorous stirring. The obtained solution was stirred for an additional 1 h to obtain a homogeneous solution and aging for 12 h to obtain CGO suspension. The iron oxide magnetic nanoparticle was prepared on the basis of previous study [41]. Briefly, 3.21 g of $NH_4Fe(SO_4)_2{\cdot}12H_2O$, 1.74 g of $(NH_4)_2SO_4{\cdot}FeSO_4{\cdot}6H_2O$ and 30 mL distilled water were mixed with vigorous stirring under N_2 atmosphere, followed by the addition of 3 mL 25% aqueous ammonia to gain a black precipitate and aging for 30 min at 85 °C to obtain iron oxide nanopaticle. After that, CGO suspension was added slowly to iron oxide dispersion at room temperature, and stirring for 45 min to obtain MCGO. Finally, the precipitate was washed several times with distilled water and dried in a vacuum oven at 50 °C. The obtained product was MCGO.

2.4. Characterization of MCGO

The morphologies of synthesized nanomaterials were characterized using scanning election microscopy (SEM) (JSM-6700FLV) and transmission electron microscopy (TEM) (Tecnai G2 F20). FT-IR spectra of samples were measured on a Fourier transform infrared (FT-IR) spectroscope (IRAffinity-1, Shimadzu, Japan) in the range of 4000–400 cm^{-1} at room temperature. X-ray diffraction (XRD) (Rigaku D/max 2500 diffractometer, Rigaku, Japan) was used to investigate the structure phases of samples.

2.5. Bacterial culture

All samples and glassware were disinfected at 121 °C for 15 min with autoclave before microbiological experiment. The bacterial strains (*E. coli* ATCC 25922) were grown in Luria-Bertani (LB) medium containing 5 g yeast extract, 10 g tryptone, 5 g NaCl and 1 L of distilled water at 37 °C with continuous shaking at 120 rpm for 24 h. The cultures were acquired by centrifugation, followed by washing three times with sterile distilled water and resuspended in sterile distilled water.

2.6. Antibacterial activity texts of MCGO

Antibacterial activity of the chitosan, GO, iron oxide nanoparticle and MCGO was investigated by exposing the *E. coil* cells in sterile distilled water containing all concentrations of the nanomaterials (50, 100, 200 μg/mL) at 37 °C under 150 rpm shaking speed at a cell concentration of 10^5–10^6 CFU/mL. A serial dilution was performed with the cells after the 0–120 min of exposure time. Amount

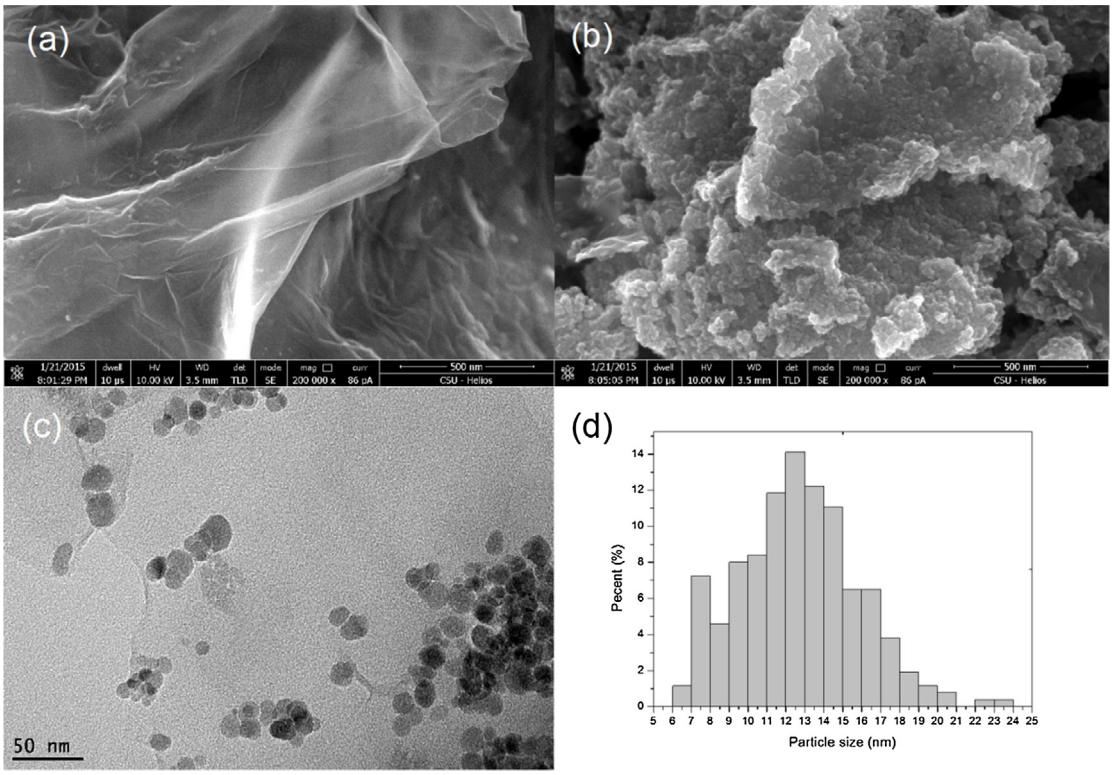

Fig. 1. SEM images of GO (a) and MCGO (b), TEM image of MCGO (c), and the size distribution MCGO (d).

of 100 mL non-diluted samples and all cell dilutions were spread onto LB media per gradient solution and incubated overnight at 37 °C. The antibacterial performance was evaluated by counting the colony-forming units (CFU).

All of the above experiments were prepared in triplicate, averages and standard deviations were calculated from triplicates and the data was normalized by using logarithm-base 10 values. The detection limit (DL) of these experiments was 10 CFU/mL.

2.7. Batch adsorption studies

Stock solutions of MO were prepared by dissolving compounds with known weight in distilled water, the pH values of the solutions were adjusted with 0.1 M NaOH and 0.1 M HCl using a pH meter. Batch adsorption experiments were carried out in 50 mL flasks with 25 mL MO aqueous solution with concentration of 50 mg/L and MCGO (0.25–2 g/L), and agitated under 150 rpm at 25 °C. The MO concentration was determined by the absorbance at 464 nm in the ultraviolet–visible (UV–vis) spectrum.

The influence of pH on MO removal by MCGO was examined in flakes containing 25 mL MO solution (50 mg/L) and 0.5 g/L MCGO under 150 rpm shaking speed at 25 °C with pH values ranging from 4 to 10. Subsequently, after 24 h shaking, the adsorbents were magnet separation and the remaining MO concentration was detected.

To determine the equilibrium contact time, samples were taken from different flasks containing 25 mL of 50 mg/L MO and 0.5 g/L MCGO at given time intervals in a shaker at 150 rpm at 25 °C. The residual MO concentration was determined.

The sorption isotherms experiments were performed in flasks containing 25 mL 0.5 g/L MCGO and MO with initial concentrations varying from 20 mg/L to 800 mg/L under 150 rpm shaking speed at 25 °C for 24 h.

3. Results and discussion

3.1. Characterization of MCGO

Fig. 1a shows a typical morphology of GO obtained by the modified Hummer's method, which presents a flake-like shapes with smooth surface, high transparency and wrinkled edge. After combination with iron oxide and chitosan, some small particles can be discernible on the MCGO composite (Fig. 1b) owing to the attached iron oxide. According to Fig. 1b, MCGO had a quite rough surface and spherical iron oxide nanocomposites were well-dispersed on the surface of the GO layers with a high density. The well-distributed iron oxide nanoparticles on the surface of GO may be attributed to the strong hydrogen bond interaction between iron oxide and active functional groups on the surface of GO [42]. As shown in the TEM image (Fig. 1c) and the histogram of the particle size distribution (Fig. 1d), the average particle size of MCGO was 12.83 ± 3.11 nm.

The FT-IR spectra of GO and MCGO were depicted in Fig. 2. According to Fig. 2, the FT-IR pattern of GO revealed the existence of the oxygen-containing functional groups. The absorption peaks at 1402, 1225, 1627 and 1732 cm^{-1} corresponded to the C=O symmetric stretching of carboxyl [43], the C—OH stretching peak [44], aromatic C=C stretching and carbonyl C=O stretching vibrations, respectively [41]. Additionally, the peak at 3413 cm^{-1} was associated with the stretching of O—H [41]. For MCGO, due to hydrogen bonding between GO and hexatomic ring of CS, the carboxyl group from GO was downshifted and assigned to the peak at 1680 cm^{-1} [45]. The peak at 1542 cm^{-1} was ascribed to C—N stretching of amide group [40], which means that CS was existed in MCGO. Furthermore, the peak at 562 cm^{-1} was assigned to the Fe—O stretching vibration [41]. The FT-IR results testified that the MCGO nanocomposite was indeed produced.

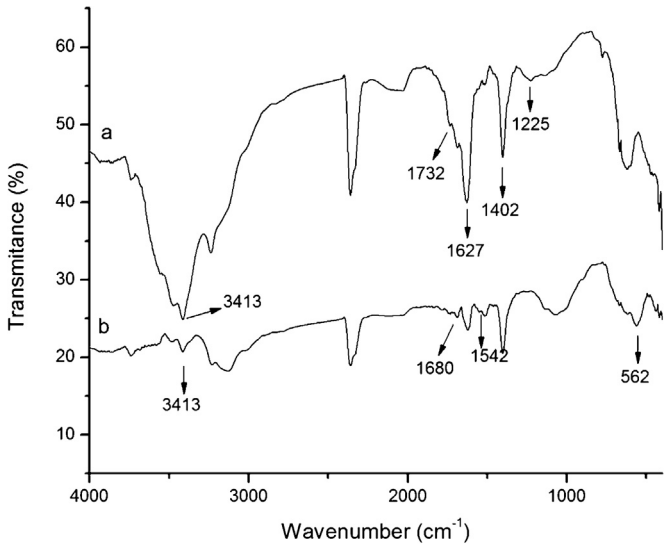

Fig. 2. FT-IR spectra of GO (a) and MCGO (b).

The XRD patterns of GO, iron oxide particles and MCGO were shown in Fig. 3. Fig. 3a showed the XRD patterns of GO, the intense diffraction peak at $2\theta = 10.1^\circ$ (0 0 1) corresponded to the typical diffraction peak of GO nanosheets. Fig. 3b and c displayed the XRD patterns of iron oxide and MCGO, respectively. As can be seen, the XRD analysis of iron oxide particles and MCGO were mostly coincident. The six characteristic diffraction peaks at $2\theta = 30.1^\circ$ (2 2 0), 35.5° (3 1 1), 43.2° (4 0 0), 53.6° (4 2 2), 57.2° (5 1 1) and 62.7° (4 4 0) were observed in iron oxide and MCGO. The four main characteristic diffraction peaks at $2\theta = 30.1^\circ$, 35.5°, 57.2° and 57.2° can be ascribed to maghemite or magnetite [46] and the other two peaks at $2\theta = 53.6^\circ$ and 62.7° were assigned to hematite [47]. Among them, the maghemite and magnetite are magnetic, which indicated that the MCGO nanocomposite had good magnetic properties and can be separated from solution easily. It was noted that the diffraction peak of GO at $2\theta = 10.1^\circ$ (0 0 1) disappeared in Fig. 3c, which could be caused by the strong peaks of iron oxide particles overwhelming the weak peaks of carbon [41,48]. Fig. 3d verified the separation convenience of MCGO. It can be seen that all the MCGO particles were separated from the solution when exposing to an external magnetic field.

3.2. Antibacterial activity of GO, CS, iron oxide nanoparticle and MCGO

Antibacterial performance of GO, CS, iron oxide nanoparticle and MCGO on bacteria was investigated using a model bacterium *E. coli*. The *E. coli* cell suspensions (10^5–10^6 CFU/mL) were incubated with these materials (100 μg/mL) for 2 h at 37 °C under 150 rpm shaking speed. A series of 100 μL cell samples were sampled at prepared time intervals and diluted to a series of 10-fold concentration gradient. Then, all cell dilutions were spread onto LB medium and incubated at 37 °C for 24 h, the inactivation was evaluated by the plate count.

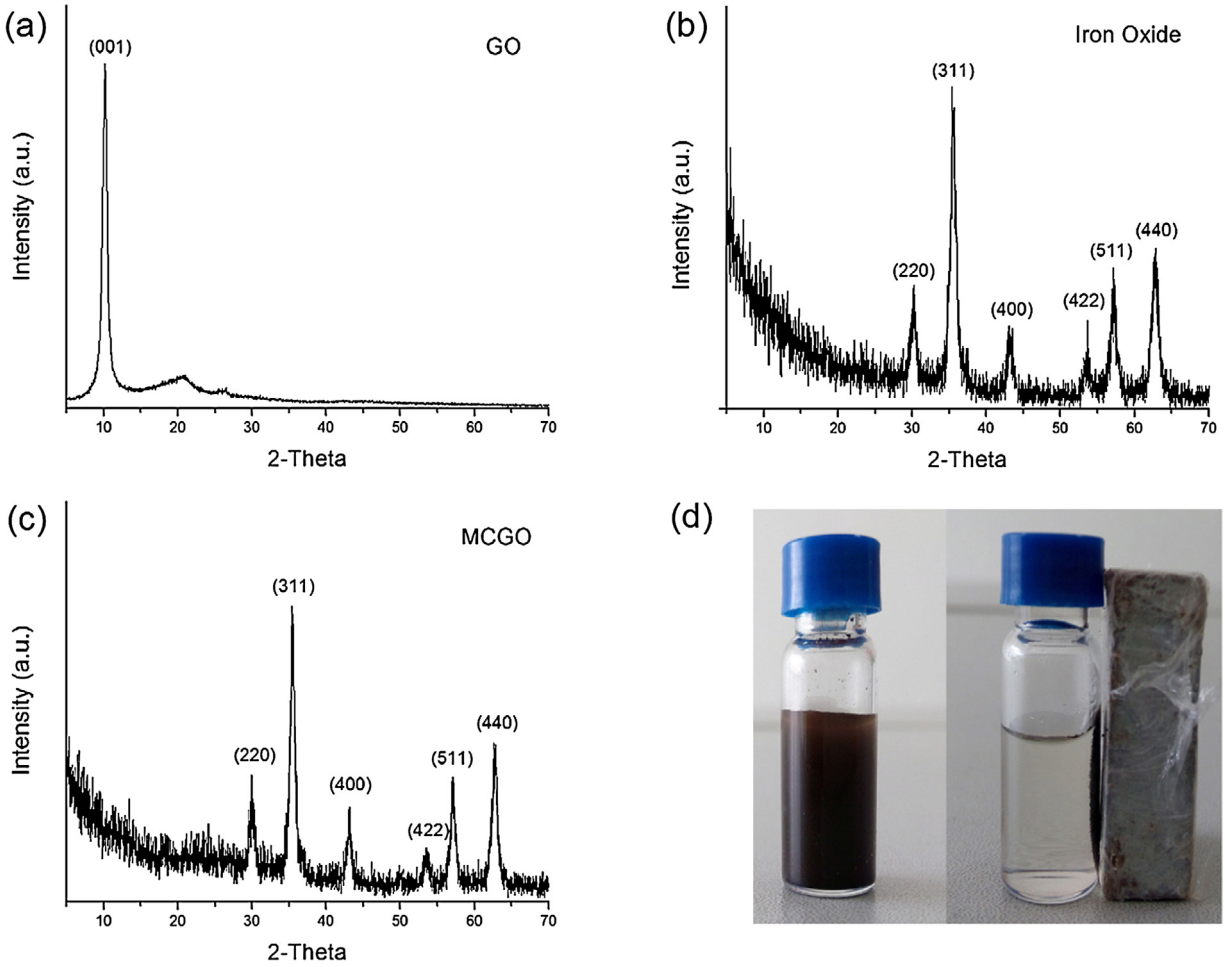

Fig. 3. XRD patterns of GO (a), iron oxide particles (b), and MCGO (c), and the MCGO dispersion and magnetic separation (d).

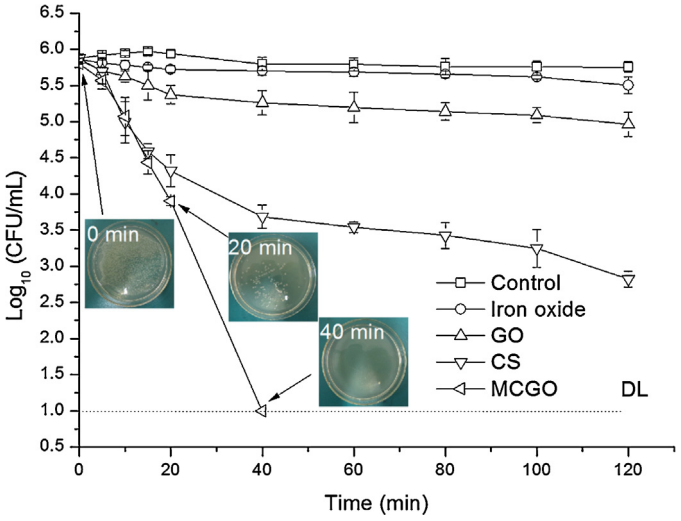

Fig. 4. Antibacterial activity of iron oxide, GO, CS and MCGO against *E. coli* bacteria, at the same concentration of 100 μg/mL at 37 °C.

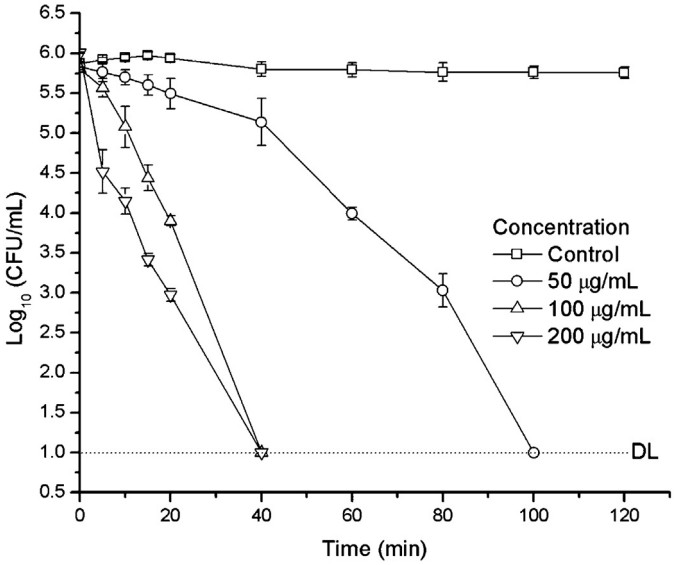

Fig. 5. Antibacterial activity after exposure to various concentrations of MCGO (50 μg/mL, 100 μg/mL, and 200 μg/mL) at 37 °C.

The antibacterial activity of GO, CS, iron oxide nanoparticle and MCGO were shown in Fig. 4. As can be seen, iron oxide nanoparticle exhibited an antibacterial activity with reduction in viable cells of 0.36 ± 0.12 log CFU/mL (inactivation percentage at 55.92 ± 9.62%) after 2 h of exposure. Similar phenomenon about antibacterial activity of magnetite (Fe_3O_4) nanoparticle was also obtained by other scientist [49]. While GO displayed a better bacterial performance to *E. coli* cells, with reduction in viable cells of 0.92 ± 0.14 log CFU/mL (inactivation percentage at 87.26 ± 3.75%) after 2 h of exposure. CS reduced the number of *E. coli* cells by 3.06 ± 0.06 log CFU/mL (inactivation percentage at 99.91 ± 0.02%), which means CS exhibited a better inactivation activity than GO and iron oxide nanoparticle. When *E. coli* cells exposed to MCGO suspension for 40 min, the bacterial concentration decreased below the DL (10 CFU/mL). Compared to iron oxide nanoparticle, GO and CS, MCGO displayed a higher inactivation percentage (98.76 ± 0.16%) than iron oxide nanoparticle (27.59 ± 3.09%), GO (67.08 ± 7.17%) and CS (97.24 ± 1.09%) after 20 min of exposure, which means the prepared MCGO possessed the strongest and fastest antibacterial performance among the four kinds of materials. To show the antibacterial activity directly, the pictures of bacterial colonies formed by *E. coli* cells treated with MCGO for 0 min, 20 min and 40 min were inserted into Fig. 4. Compared to the control sample with 0 min of exposure, MCGO showed a high bacterial activity with few bacterial colonies existed on LB-ager plate after 20 min of exposure and no more cells viable after 40 min of contact.

Sreeprasad et al. [50] anchored different materials such as native lactoferrin (NLf) or NLf protected Au cluster (Au@NLf) and/or chitosan (Ch) into GO/RGO to synthesis multifunctional composites. They found that owing to the synergetic effect of the combination of materials, these multifunctional composites exhibited higher antibacterial activity than GO/RGO. Wang et al. [51] synthesized the ZnO/GO composite, they reported the antibacterial activity of ZnO/GO composite mainly due to the synergistic effect of ZnO and GO. Ma et al. [52] also reported silver-modified graphene oxide nanosheets exhibited higher antibacterial activity toward *E. coli* compared to both silver nanopatricle and GO due to the synergistic effect of GO and silver nanoparticle. Noticeably, the enhanced antibacterial activity of MCGO compared with iron oxide, GO and CS in our work might dependent on the synergistic effect of iron oxide, GO and CS.

3.3. Effect of concentration on antibacterial activity

The *E. coli* cells were exposed to different concentrations of MCGO nanoparticles (50 μg/mL, 100 μg/mL and 200 μg/mL), the inactivation was appraised by the plate count and the concentration effect on antimicrobial activity was displayed in Fig. 5. According to Fig. 5, the toxic effect and sterilization rate toward the *E. coli* cells were increased with the increasing concentration of MCGO. It was noticed that, the reduction in viable cells at 20 min increased 0.36 ± 0.16 log CFU/mL (with 53.85 ± 15.39% inactivation percentage), 1.91 ± 0.05 log CFU/mL (with 98.76 ± 0.16% inactivation percentage), and 3.04 ± 0.07 log CFU/mL (with 99.91 ± 0.02% inactivation percentage), for exposure to MCGO suspensions at the concentrations of 50 μg/mL, 100 μg/mL and 200 μg/mL, respectively. After exposure to MCGO suspension at the concentration of 50 μg/mL, the bacterial concentration decreased below the DL at 100 min. While, after incubation with MCGO suspensions at the concentrations of 100 and 200 μg/mL, the bacterial concentration decreased below the DL at 40 min. Furthermore, it was observed that the loss of cell viability was escalated with the increase of exposure time when incubated at given material concentration. Therefore, our results indicated that the antibacterial capacity of MCGO was not only concentration dependent but also time dependent.

Our previous research in terms of *E. coli* exposure to iron oxide loaded graphene nanocomposites demonstrated that the percentage of cell death was escalated with increasing concentration of material from 30 μg/mL to 300 μg/mL, and there were no cell live when exposed in 200 μg/mL material concentration with 2 h incubation [41]. Similar results were also obtained by other scientists [25,53,54]. They found that the antibacterial capacity increased with the increasing concentration of material and the microbial inactivation increased with the increasing exposure time.

3.4. Cell membrane damage of bacteria exposed to MCGO

To better understand the interaction between *E. coli* cells and MCGO nanocomposites, the SEM analysis of cells before and after exposure to 100 μg/mL of the nanocomposites was conducted to investigate the changes of cell morphology. As revealed in SEM images (Fig. 6), compared to the cells before exposure to nanomaterials, which exhibited a rod shape and maintained the integrity

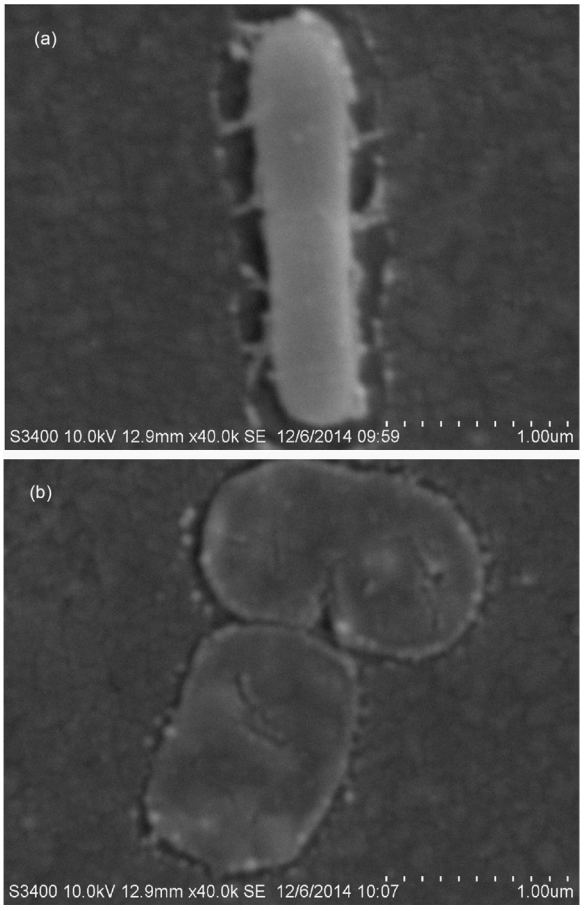

Fig. 6. SEM images of *E. coli* cell before (a) and after (b) exposure to MCGO.

of cells (Fig. 6a), the cells' membranes deformed after treated with MCGO and there were pronounced breakages on the membranes (Fig. 6b). Similar phenomena were discovered by other researchers [55,56]. The mechanism of bacterial cytotoxicity might be directly caused by membrane damage. The breakages of the membranes might cause the leakage of intracellular components out of cell membrane, and result in the death of bacterial cells. According to previous studies, the interaction between positively charged chitosan and the negatively charged membrane of cells altered the cell permeability and led to the leakage of intracellular constituents [57]. Additionally, GO can lead to the damage of cell structures by inducing membrane stress [25,54]. Moreover, iron oxide nanoparticle generated reactive oxygen species (ROS) when interacting with bacteria, leading to protein oxidation and DNA damage, and finally resulting in cells death [58,59]. Hence, the antibacterial properties of MCGO might be related to the synergistic effect of iron oxide, GO and CS.

3.5. Methyl orange adsorption

3.5.1. Effect of adsorbent mass

The effect of MCGO dosage on MO adsorption was investigated by varying dosages from 0.25 to 2 g/L, and the adsorption percentage and adsorbed amount of MO was presented in Fig. 7. It was observed that the adsorption percentage increased from 56.0% to 88.4% with increasing adsorbent mass from 0.25 to 2 g/L. An increasing trend in percentage of MO removal might be caused by the increased surface area and active functional groups, which increase the availability of active adsorption sites [42,60]. It was also observed from Fig. 7 that the adsorption capacity decreased

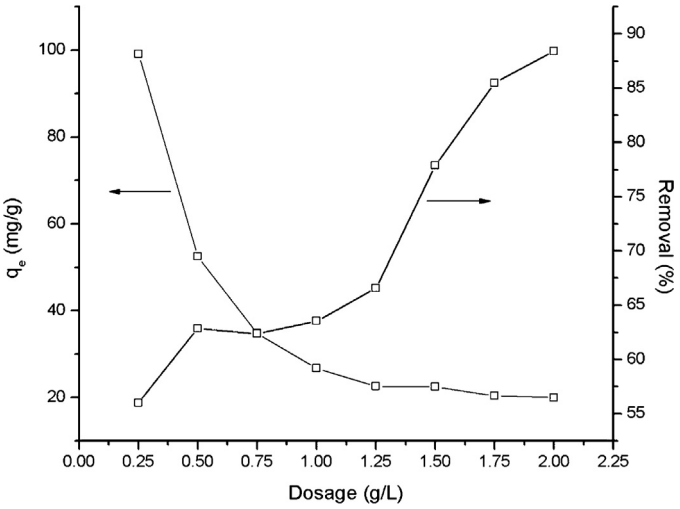

Fig. 7. Adsorption capacity and percentage of removal for MO adsorption of MCGO with different adsorbent dosages.

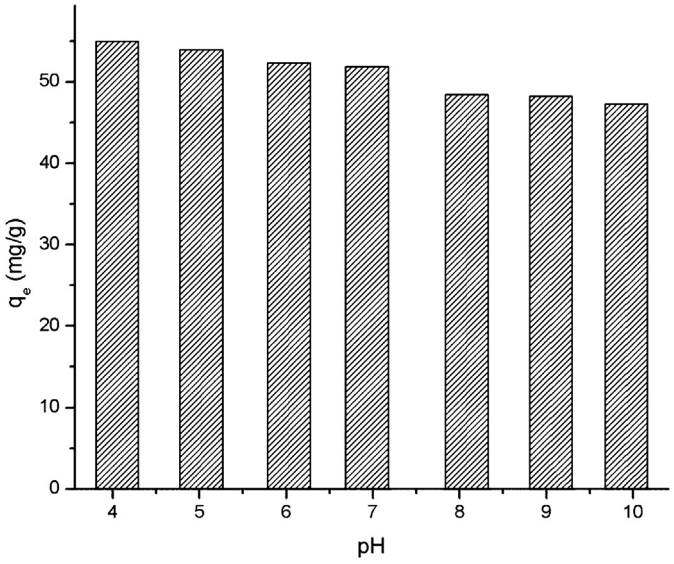

Fig. 8. Effect of pH on the adsorption of MO by MCGO.

with increasing adsorbent mass. The decrease in adsorption capacity of MO removal might be due to the fact that with increasing adsorbent dosage, the active adsorption sites could not all be covered by MO molecules and could not reach equilibration.

3.5.2. Effect of pH

The pH is an important factor of the adsorption process as it affects surface charge of the adsorbent and the protonation degree of the functional groups [28]. Fig. 8 depicted the effect of pH on MO removal. It was found that the adsorbed amount of MO by MCGO weakly decreased by increasing the initial pH from 4 to 10 and the highest adsorption efficiency was found to be at the initial pH 4. As depicted in Fig. 9, the zeta potential of MCGO decreased since pH increased, and the isoelectric point of MCGO was about 10. Thus, the positively charged MCGO (pH < 10) resulted in a favorable electrostatic attraction to anionic dye (MO). Consequently, the adsorption mechanism was influenced by electrostatic interactions between the anionic dye MO and the cationic groups of MCGO.

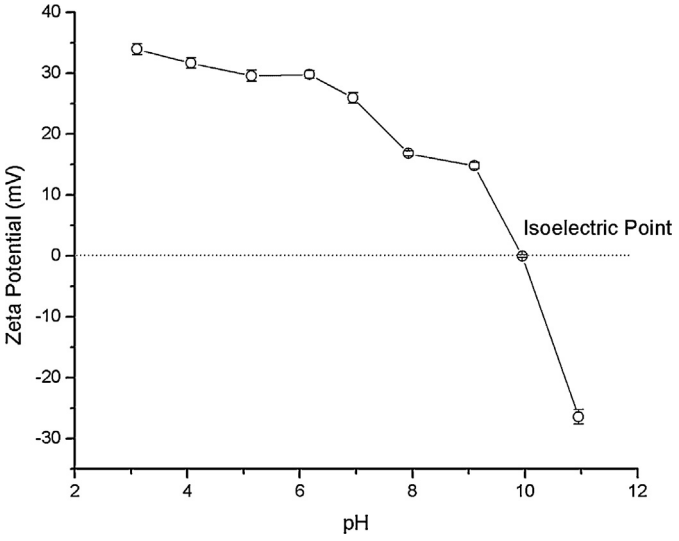

Fig. 9. Zeta potentials of MCGO at various pH values.

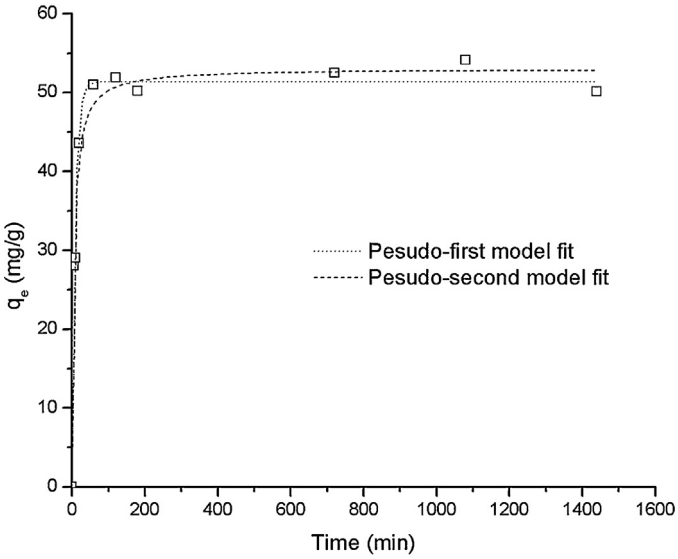

Fig. 10. Effect of contact time and model fits of pseudo-first-order model and pseudo-second-order model on the adsorption capacity for MO adsorption of MCGO.

3.5.3. Effect of contact time

To illustrate the adsorption mechanism and kinetics, the pseudo-first-order and pseudo-second-order kinetic models were used to determine the kinetics of MO adsorption on the MCGO.

The pseudo-first-order kinetic model is one of the most widely used equations to describe the adsorption rate based on the adsorption capacity. The kinetic model is expressed by the following equation:

$$\log(Q_e - Q_t) = \log Q_e - \frac{k_1}{2.303}t \quad (1)$$

where k_1 is the adsorption rate constant (min^{-1}), and Q_e and Q_t are the amounts of MO adsorbed at equilibrium and time t (min), respectively.

The pseudo-second-order kinetic model is based on the adsorption capacity of the dye molecules on the surface of the adsorbent and used to simulate the kinetic sorption. The kinetic model is expressed as follows:

$$\frac{t}{Q_t} = \frac{1}{k_2 {Q_e}^2} + \frac{1}{Q_e}t \quad (2)$$

where k_2 is the rate constant of pseudo-second-order adsorption, Q_e and Q_t are the adsorbed amount of adsorbate at equilibrium and time t (min), respectively.

The effect of contact time on the adsorption of MO by MCGO was displayed in Fig. 10. As can be seen, the adsorption rate increased dramatically at the initial stage (0–60 min) and the adsorbed amount of MO reached 50.98 mg/g when the initial MO concentration was 50 mg/L. Then, the adsorbed amount of MO was fluctuating slightly and achieved equilibrium at about 180 min. The rapid adsorption in the initial stage revealed that there might be a large number of adsorption sites on MCGO, which displayed a strong affinity between MO and MCGO. After a fast adsorption stage, the repulsion between the solute molecules hindered the binding of MO molecules and remaining adsorption sites, which resulting in a slight fluctuation of adsorbed amount and a relatively long time to reach equilibrium [29]. Table 1 showed the kinetic parameters fitting to pseudo-first-order and pseudo-second-order equations. According to the correlation coefficients (R^2), the pseudo-second-order equation provided a better fit for the experimental data (R^2 = 0.9763) than the data resulted from pseudo-first-order equation (R^2 = 0.9653).

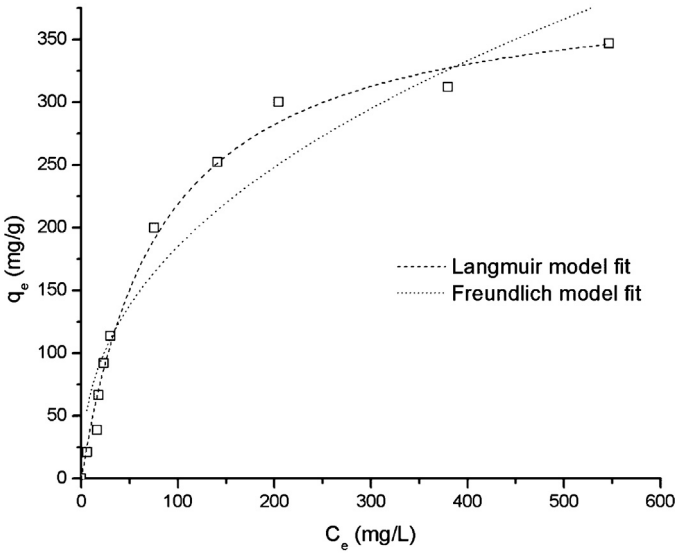

Fig. 11. Model fits of the Langmuir isotherm model and Freundlich isotherm model for the adsorption of MO by MCGO.

3.5.4. Isotherm study

To well-understand the interactive behavior between adsorbate and MCGO and predict the adsorption capacity, Langmuir and Freundlich sorption isotherm models were used to investigate the isotherm for MO adsorption on MCGO.

The equations of the Langmuir isotherm can be expressed as:

$$\frac{C_e}{Q_e} = \frac{1}{(K_L Q_m)} + \frac{C_e}{Q_m} \quad (3)$$

where Q_e (mg/g) is the adsorbed value of MO at equilibrium, Q_m (mg/g) is the maximum adsorption capacity, C_e (mg/L) is the equilibrium concentration of MO in solution, and K_L ($L mg^{-1}$) is the Langmuir constant, which is related to adsorption energy.

The equation of the Freunlich isotherm can be expressed as:

$$\ln\ Q_e = \ln K_F + \left(\frac{1}{n}\right) \ln\ C_e \quad (4)$$

where Q_e (mg/g) is the adsorbed value of MO at equilibrium, C_e (mg/L) is the equilibrium concentration of MO in solution, K_F and n

Table 1
Determined constants and correlation coefficients (R^2) of pseudo-first (second)-order kinetic models.

Pseudo-first-order			Pseudo-second-order		
k_1 (min^{-1})	$Q_{e,1}$ (mg/g)	R^2	k_2 ($g\,mg^{-1}\,min^{-1}$)	$Q_{e,2}$ (mg/g)	R^2
0.10653	51.361	0.9653	0.00344	53.035	0.9763

Table 2
Parameters for Langmuir and Freundlich isotherm models.

Langmuir			Freundlich		
Q_m (mg/g)	k_L ($L\,mg^{-1}$)	R^2	n	k_F ($L\,mg^{-1}$)	R^2
398.083	0.0122	0.9897	2.3615	26.3626	0.9112

Table 3
Adsorption capacities of MO on various adsorbents.

Adsorbents	Q_m (mg/g)	Reference
γ-Fe_2O_3/SiO_2/chitosan composite	34.29	[61]
Ammonium-functionalized silica nanoparticle	105.4	[62]
Cu/Cu_2O nanocomposite	344.84	[63]
Acid modified carbon coated monolith	147.05	[64]
Heterogenized Mn nanoparticle	246.8	[65]
MCGO	398.08	This study

are Freundlich constants, which indicating the adsorption capacity and intensity factors, respectively.

The experimental data and model fits of Langmuir and Freundlich isotherms for MO was presented in Fig. 11, and the corresponding values of two isotherm models were listed in Table 2.

It can be found that the Langmuir isotherm better described the adsorption of MO with the higher regression coefficient R^2 (0.9897) than Freunlich isotherm (R^2 = 0.9112), which could be assumed that the surface of the adsorbent was homogenous and all adsorption sites had equal adsorbate affinity. Benefit from the large surface area of GO and the amino functional groups of CS, the MCGO has a higher adsorption capacity (Q_m = 398.08 mg/g) to MO than the reported values of other adsorbents (listed in Table 3).

To determine the favorability of adsorption process, a dimensionless equilibrium parameter was defined as:

$$R_L = \frac{1}{1 + K_L C_0} \quad (5)$$

where K_L ($L\,mg^{-1}$) is the Langmuir constant, and C_0 (mg/L) is the initial MO concentration. The value of R_L represents the type of the isotherm to be favorable when the value is within the range of 0–1. In this study, the value of R_L (0.0929) was within the range of 0–1, indicating that the adsorption of MO onto MCGO was a favorable process.

4. Conclusions

MCGO nanocomposite was synthesized as a multi-functional material and simultaneously used for antibacterial and removal of methyl orange. MCGO showed a high and fast antibacterial activity and almost no cell alive for 40 min exposure time with 200 μg/mL material concentration. The mechanism of bacterial cytotoxicity of MCGO toward *E. coli* may be relying on the membrane damage. Study of adsorption showed that the adsorption capacity of MCGO decreased with the increasing pH values. The adsorption of MO was fitted the pseudo-second-order kinetic model and Langmuir isotherm very well. The maximum adsorption capacity of MCGO for MO was 398.08 mg/g. Thus, the outstanding adsorption and antibacterial ability of MCGO, as well as its separation-convenient property, offers potential applications for water treatments.

Acknowledgments

The authors are grateful for the financial supports from National Natural Science Foundation of China (51521006, 51579095, 51378190, 21275044), the Program for Changjiang Scholars and Innovative Research Team in University (IRT-13R17), China National Science and Technology Support Program (2011BAE06A01), Hunan Province University Innovation Platform Open Fund Project (14K020), the Interdisciplinary Research Funds for Hunan University (531107040761) and the Scientific Research Foundation for the Returned Overseas Chinese Scholars, State Education Ministry (2013693).

References

[1] Z. Fan, B. Liu, J. Wang, S. Zhang, Q. Lin, P. Gong, L. Ma, S. Yang, Adv. Funct. Mater. 24 (2014) 3933–3943.
[2] B. Lu, T. Li, H. Zhao, X. Li, C. Gao, S. Zhang, E. Xie, Nanoscale 4 (2012) 2978–2982.
[3] L. Liu, C. Li, C. Bao, Q. Jia, P. Xiao, X. Liu, Q. Zhang, Talanta 93 (2012) 350–357.
[4] K.C. Kemp, H. Seema, M. Saleh, N.H. Le, K. Mahesh, V. Chandra, K.S. Kim, Nanoscale 5 (2013) 3149–3171.
[5] D.S. Su, S. Perathoner, G. Centi, Chem. Rev. 113 (2013) 5782–5816.
[6] W.S. Wan Ngah, I.M. Isa, J. Appl. Polym. Sci. 67 (1998) 1067–1070.
[7] Y.-B. Wu, S.-H. Yu, F.-L. Mi, C.-W. Wu, S.-S. Shyu, C.-K. Peng, A.-C. Chao, Carbohydr. Polym. 57 (2004) 435–440.
[8] L. Qi, Z. Xu, X. Jiang, C. Hu, X. Zou, Carbohydr. Res. 339 (2004) 2693–2700.
[9] F.-C. Wu, R.-L. Tseng, R.-S. Juang, Water Res. 35 (2001) 613–618.
[10] S. Babel, T.A. Kurniawan, J. Hazard. Mater. 97 (2003) 219–243.
[11] Q. Li, S. Mahendra, D.Y. Lyon, L. Brunet, M.V. Liga, D. Li, P.J. Alvarez, Water Res. 42 (2008) 4591–4602.
[12] N. Bhattarai, D. Edmondson, O. Veiseh, F.A. Matsen, M. Zhang, Biomaterials 26 (2005) 6176–6184.
[13] C. Charan, V.K. Shahi, J. Appl. Electrochem. 44 (2014) 953–962.
[14] L. Higueras, G. López-Carballo, R. Gavara, P. Hernández-Muñoz, Food Bioprocess Technol. 8 (2014) 526–538.
[15] M.-S. Chiou, H.-Y. Li, J. Hazard. Mater. 93 (2002) 233–248.
[16] Y.C. Chang, D.H. Chen, J. Colloid Interface Sci. 283 (2005) 446–451.
[17] L. Jin, R. Bai, Langmuir 18 (2002) 9765–9770.
[18] P.K. Dutta, S. Tripathi, G.K. Mehrotra, J. Dutta, Food Chem. 114 (2009) 1173–1182.
[19] L.-Y. Zheng, J.-F. Zhu, Carbohydr. Polym. 54 (2003) 527–530.
[20] C. Qin, H. Li, Q. Xiao, Y. Liu, J. Zhu, Y. Du, Carbohydr. Polym. 63 (2006) 367–374.
[21] Y. Wang, X. Liu, H. Wang, G. Xia, W. Huang, R. Song, J. Colloid Interface Sci. 416 (2014) 243–251.
[22] K.S. Novoselov, A.K. Geim, S.V. Morozov, D. Jiang, Y. Zhang, S.V. Dubonos, I.V. Grigorieva, A.A. Firsov, Science 306 (2004) 666–669.
[23] G.K. Ramesha, A.V. Kumara, H.B. Muralidhara, S. Sampath, J. Colloid Interface Sci. 361 (2011) 270–277.
[24] T. Wu, X. Cai, S. Tan, H. Li, J. Liu, W. Yang, Chem. Eng. J. 173 (2011) 144–149.
[25] O. Akhavan, E. Ghaderi, ACS Nano 4 (2010) 5731–5736.
[26] C. Santhosh, P. Kollu, S. Doshi, M. Sharma, D. Bahadur, M.T. Vanchinathan, P. Saravanan, B.-S. Kim, A.N. Grace, RSC Adv. 4 (2014) 28300.
[27] S. Chella, P. Kollu, E.V.P.R. Komarala, S. Doshi, M. Saranya, S. Felix, R. Ramachandran, P. Saravanan, V.L. Koneru, V. Venugopal, S.K. Jeong, A. Nirmala Grace, Appl. Surf. Sci. 327 (2015) 27–36.
[28] I.E. Mejias Carpio, J.D. Mangadlao, H.N. Nguyen, R.C. Advincula, D.F. Rodrigues, Carbon 77 (2014) 289–301.
[29] Y. Wang, G. Xia, C. Wu, J. Sun, R. Song, W. Huang, Carbohydr. Polym. 115 (2015) 686–693.
[30] Y. Xu, Q. Dang, C. Liu, J. Yan, B. Fan, J. Cai, J. Li, Colloids Surf. A: Physicochem. Eng. Asp. 482 (2015) 353–364.

[31] D.-W. Cho, B.-H. Jeon, C.-M. Chon, F.W. Schwartz, Y. Jeong, H. Song, J. Ind. Eng. Chem. 28 (2015) 60–66.
[32] Y. Haldorai, D. Kharismadewi, D. Tuma, J.-J. Shim, Korean J. Chem. Eng. 32 (2015) 1688–1693.
[33] L. Fan, C. Luo, M. Sun, X. Li, F. Lu, H. Qiu, Bioresour. Technol. 114 (2012) 703–706.
[34] L. Fan, C. Luo, X. Li, F. Lu, H. Qiu, M. Sun, J. Hazard. Mater. 215–216 (2012) 272–279.
[35] L. Fan, C. Luo, M. Sun, X. Li, H. Qiu, Colloids Surf. B: Biointerfaces 103 (2013) 523–529.
[36] O. Akhavan, E. Ghaderi, Carbon 50 (2012) 1853–1860.
[37] A.A. Jalil, S. Triwahyono, S.H. Adam, N.D. Rahim, M.A. Aziz, N.H. Hairom, N.A. Razali, M.A. Abidin, M.K. Mohamadiah, J. Hazard. Mater. 181 (2010) 755–762.
[38] W.S. Hummers, R.E. Offeman, J. Am. Chem. Soc. 80 (1958) 1339.
[39] Y. Chen, L. Chen, H. Bai, L. Li, J. Mater. Chem. A 1 (2013) 1992–2001.
[40] H.M. Hegab, Y. Wimalasiri, M. Ginic-Markovic, L. Zou, Desalination 365 (2015) 99–107.
[41] C.H. Deng, J.L. Gong, G.M. Zeng, C.G. Niu, Q.Y. Niu, W. Zhang, H.Y. Liu, J. Hazard. Mater. 276 (2014) 66–76.
[42] S. Sheshmani, A. Ashori, S. Hasanzadeh, Int. J. Biol. Macromol. 68 (2014) 218–224.
[43] V. Erukhimovitch, L. Tsror, M. Hazanovsky, M. Talyshinsky, I. Mukmanov, Y. Souprun, M. Huleihel, J. Agric. Technol. 1 (2005) 145–152.
[44] H. Hu, X. Wang, J. Wang, F. Liu, M. Zhang, C. Xu, Appl. Surf. Sci. 257 (2011) 2637–2642.
[45] D. Han, L. Yan, W. Chen, W. Li, Carbohydr. Polym. 83 (2011) 653–658.
[46] J.L. Gong, B. Wang, G.M. Zeng, C.P. Yang, C.G. Niu, Q.Y. Niu, W.J. Zhou, Y. Liang, J. Hazard. Mater. 164 (2009) 1517–1522.
[47] M. Legodi, D. Dewaal, Dyes Pigments 74 (2007) 161–168.
[48] X. Yang, C. Chen, J. Li, G. Zhao, X. Ren, X. Wang, RSC Adv. 2 (2012) 8821.
[49] C. Ramteke, B.K. Sarangi, T. Chakrabarti, S. Mudliar, D. Satpute, R.A. Pandey, Curr. Nanosci. 6 (2010) 587–591.
[50] T.S. Sreeprasad, M.S. Maliyekkal, K. Deepti, K. Chaudhari, P.L. Xavier, T. Pradeep, ACS Appl. Mater. Interfaces 3 (2011) 2643–2654.
[51] Y.W. Wang, A. Cao, Y. Jiang, X. Zhang, J.H. Liu, Y. Liu, H. Wang, ACS Appl. Mater. Interfaces 6 (2014) 2791–2798.
[52] J. Ma, J. Zhang, Z. Xiong, Y. Yong, X.S. Zhao, J. Mater. Chem. 21 (2011) 3350–3352.
[53] Y. Pan, H. Bao, L. Li, ACS Appl. Mater. Interfaces 3 (2011) 4819–4830.
[54] S. Liu, T.H. Zeng, M. Hofmann, E. Burcombe, J. Wei, R. Jiang, J. Kong, Y. Chen, ACS Nano 5 (2011) 6971–6980.
[55] W. Hu, C. Peng, W. Luo, X. Li, D. Li, Q. Huang, C. Fan, ACS Nano 4 (2010) 4317–4323.
[56] C. Yang, J. Mamouni, Y. Tang, L. Yang, Langmuir: ACS J. Surf. Colloids 26 (2010) 16013–16019.
[57] E.I. Rabea, M.E.-T. Badawy, C.V. Stevens, G. Smagghe, W. Steurbaut, Biomacromolecules 4 (2003) 1457–1465.
[58] N. Tran, A. Mir, D. Mallik, A. Sinha, S. Nayar, T.J. Webster, Int. J. Nanomed. 5 (2010) 277–283.
[59] B. Stephen Inbaraj, T.-Y. Tsai, B.-H. Chen, Sci. Technol. Adv. Mater. 13 (2012) 015002.
[60] Q. Du, J. Sun, Y. Li, X. Yang, X. Wang, Z. Wang, L. Xia, Chem. Eng. J. 245 (2014) 99–106.
[61] H.Y. Zhu, R. Jiang, Y.Q. Fu, J.H. Jiang, L. Xiao, G.M. Zeng, Appl. Surf. Sci. 258 (2011) 1337–1344.
[62] J. Liu, S. Ma, L. Zang, Appl. Surf. Sci. 265 (2013) 393–398.
[63] T. Kou, Y. Wang, C. Zhang, J. Sun, Z. Zhang, Chem. Eng. J. 223 (2013) 76–83.
[64] W. Cheah, S. Hosseini, M.A. Khan, T.G. Chuah, T.S.Y. Choong, Chem. Eng. J. 215–216 (2013) 747–754.
[65] M. Arshadi, M. Mehravar, M.J. Amiri, A.R. Faraji, J. Colloid Interface Sci. 440 (2015) 189–197.